DNS-BASED THERMOHYDRAULIC ASSESSMENT OF ARTIFICIAL ROUGHNESS SURROGATES

J. Yang,[1,*] J. Velandia,[2,3] S. Bansmer,[2,3] A. Stroh,[1] P. Forooghi[4]

[1]Institute of Fluid Mechanics, Karlsruhe Institute of Technology, Karlsruhe, 76131, Germany
[2]Institut für Strömungsmechanik, Technische Universität Braunschweig, Hermann-Blenk-Str.37, Braunschweig, 38108, Germany
[3]Coldsense Technologies, Hermann-Blenk-Str.37, Braunschweig, 38108, Germany
[4]Deparment of Mechanical & Production Engineering, Aarhus University, Katrinebjergvej 89G-F, Aarhus, 8200, Denmark

ABSTRACT

Engineering-related surfaces are commonly rough to different extent. In contrast to smooth surfaces, turbulent flows over rough surfaces exhibit enhanced heat and momentum transfer in the near-wall region due to surface undulation. A long-standing research question in this field is how to predict the roughness effect based solely on its topographical properties. In this regard, a large body of research devoted to characterizing roughness topographies has demonstrated that the usage of reduced statistical properties like skewness or effective slope of the surface remains insufficient to recover the overall roughness effect. Having this in mind, we discuss the potential of characterizing the roughness effect on the temperature field based on the roughness height probability density function (PDF) and power spectrum (PS) in the present contribution. Hereby, different types of realistic roughness from various engineering applications are considered. A mathematical roughness reproduction method is utilized to generate artificial rough surfaces based on the realistic PDF and PS. The artificially reproduced surfaces are subsequently compared with their original surfaces in terms of the thermal properties. For this purpose, direct numerical simulations (DNS) of flow over the roughness are carried out in a fully developed turbulent channel flow at friction Reynolds number Re_τ =500 - 2000 to cover different rough regimes. Successful reproduction of the flow statistics by the artificial roughness surrogates indicates the feasibility of the current roughness characterization/reproduction method. Less than 4% discrepancies in the global flow statistics are achieved. However, the present roughness reproduction framework is shown not applicable for the roughness with strong surface anisotropy.

KEY WORDS:

1. INTRODUCTION

The critical role of the roughness in altering the engineering surface performance can be attributed to the enhanced momentum and heat transfer intensity in the near wall region. Based on the outer-layer similarity hypothesis proposed by Townsend [1], under the circumstance of a significant separation of scales between roughness height k and boundary layer height δ, i.e. $\delta \gg k$, the flow in the outer layer remains unaffected by the roughness. It is widely accepted, that a shift of the mean velocity and temperature profiles compared to the

*Corresponding J. Yang: jiasheng.yang@kit.edu

smooth surface is expected in the logarithmic layer with a wall-normal offset for the flow subjected to roughness. The mean velocity and temperature wall-normal offset in the logarithmic layer, denoted as the roughness function ΔU^+ [2] and temperature roughness function $\Delta \Theta^+$ [3], respectively, can be used to quantify the enhancement of skin fiction and heat transfer imposed by a roughness [4].

Engineering prediction of surface roughness is generally characterized by the equivalent sand grain height k_s [5]. Obtaining this value for a roughness of interest is an expensive practice, since either experiments or high-fidelity simulations are required. Many attempts have been performed in order to find the k_s value solely based on roughness topographical features. In preceding investigations, a number of roughness topographical statistics are suggested to characterize the roughness, e.g. the skewness Sk or the effective slope ES [6, 7]. However, to the best knowledge of authors, there is not a single, or a combination of roughness parameter(s) that is capable for precisely recover the roughness effect. There is widely reported evidence that roughness structures exhibit a different effect on the flow at different roughness length scales. Barros *et al.* [8] and Busse *et al.* [9] applied high- and low-pass filtering to an irregular roughness and identified different mechanism of the roughness impact on the flow at different roughness length scales. Moreover, Yang *et al.* [10] analyzed the coherence function between local surface force and the roughness structure, coming to the conclusion that the small roughness length scales are more prone to exerting the surface drag force onto the flow. To quantify the respective augmentation of heat and momentum transfer exerted by roughness, [11] proposed Reynolds analogy factor $RA = 2St/C_f$, where St and C_f represent Stanton number and skin friction coefficient, respectively. It is established that the Reynolds analogy of a flow over roughness is strongly affected by the topography of rough surface [12]. Additionally, Nusselt number Nu is usually used to reflect the roughness heat transfer ability. Heat transfer over roughness – both via experiments and simulations – are studied by a number of researchers. Bons and McClan [13] studied heat transfer of different types of degraded turbine surfaces. A systematic study of roughness heat transfer with varied roughness topography is conducted by Forooghi *et al.* [14].

One of the difficulties in the area of rougness research is the inaccessibility of realistic roughness scans combined with the lack of flexibly adjustable topographical parameters. Busse *et al.* [15] employed moving average process to generated near-Gaussian irregular roughness. Flack *et al* [16] investigated non-Gaussian irregular roughness obtained by a modified version of this generation method. However, to the best knowledge of authors, the question whether an artificially generated irregular roughness can be regarded as a surrogate of realistic surfaces is still unclear. The current work serves as an attempt to answer this question by employing a mathematical roughness generation method proposed by Pérez-Ràfols and Almqvist [17] based on the roughness power spectrum (PS) and the height probability density function (PDF). Six realistic rough surfaces, which originate from 3 different engineering applications – ice accretion roughness, deposition and sandpaper – are included in the present work.

2. METHODOLOGY

2.1 Roughness generation

The sandpaper ISO Grit P60 is adopted as a generic representation of the 'naturally-occurring' roughness. In the following content, the realistic and artificial roughness associated with the sandpaper roughness are denoted as $Sand$. The ice accretion roughness on a simplified aero-engine nacelle are generated in the Braunschweig Icing Wind Tunnel [18, 19]. An overview of the ice accretion surface across pressure side, stagnation area and suction side is illustrated in figure 1. The effective slope (ES) of the surface in z-direction of figure 1 is used to identify homogeneous roughness regions. Under the assumption of homogeneous roughness, the roughness patches $ICE1$-4 are adopted in the present work. The differences in the roughness topographical properties in different regions can be attributed to the difference in the physics of the roughness formation process[18]. Another instance studied in this work is the CCD surface [20], which is extracted from the piston head of
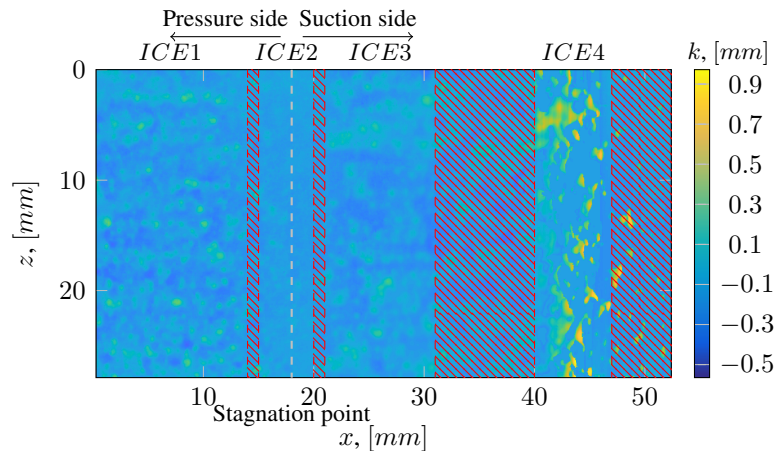
Fig. 1 Ice accretion surface, the section $ICE2$ corresponds to the stagnation region of the surface, dashed gray line indicates the stagnation point. Hatched patterns indicate transitional roughness structures.

a single-cylinder research internal combustion engine under realistic operating condition. The roughness is adopted from the previous research by Forooghi *et al.* [20].

The realistic roughness patches are represented through a discretized wall elevation map as a function of wall-parallel coordinates. Following the roughness generation method, the PDF and the PS of realistic surfaces are extracted for reproduction of their artificial surrogates. Radial averaging process of the 2D PS around the origin, i.e. around $(q_x, q_z) = (0, 0)$, is applied to generate isotropic roughness. Subsequently, moving average along the resulting 1D PS is applied to extract characteristic feature of investigated roughness PS. The eventually reproduced roughness is illustrated in the figure 3 and 4 along with their original realistic counterparts. In the following content, the realistic surfaces and its artificial surrogates are labeled with $-R$ and $-A$, respectively. Complementary, the influence of roughness PDF in determining the roughness heat transfer ability and skin friction is investigated by generating artificial roughness with matched PS but Gaussian PDF. The k_{rms} values of Gaussian PDF are set consistent with realistic PDF. These Gaussian artificial rough surfaces are labeled with $-G$ and shown in figure 4 as well. The summary of the roughness statistical metrics of the realistic and artificial roughness, including Gaussian roughness, is documented in table 1. Where the surface anisotropy ratio, SAR, is the ratio of streamwise and spanwise correlation length $SAR = L_x^{Corr}/L_z^{Corr}$ [21]. L^{Corr} is the correlation length at which distance the auto-correlation function drops under 0.2. As can be seen, while the artificial surrogates successfully reproduce the topographical statistics, the Gaussian roughness show considerable discrepancies.

Table 1 Summary of surface geometrical statistics. Units: mm.

Configuration	Surface	k_{rms}	k_{md}	k_t	Sk	ES	SAR	Surface	k_{rms}	k_{md}	k_t	Sk	ES	SAR
Realistic	$ICE1$-R	0.07	0.19	0.63	0.76	0.16	0.88	$ICE4$-R	0.17	0.26	0.98	1.87	0.40	1.68
Realistic PDF+PS	$ICE1$-A	0.07	0.19	0.63	0.76	0.17	1.00	$ICE4$-A	0.17	0.25	0.97	1.88	0.34	1.00
Gaussian PDF+PS	$ICE1$-G	0.07	0.30	0.64	0.00	0.18	1.00	$ICE4$-G	0.17	0.61	1.18	0.00	0.42	0.96
Realistic	$ICE2$-R	0.03	0.09	0.28	1.17	0.13	1.14	Sand-R	0.09	0.65	1.16	0.77	0.48	1.03
Realistic PDF+PS	$ICE2$-A	0.03	0.09	0.28	1.18	0.11	0.96	Sand-A	0.09	0.65	1.16	0.74	0.47	1.00
Gaussian PDF+PS	$ICE2$-G	0.03	0.13	0.27	0.00	0.12	0.96	Sand-G	0.09	0.84	1.29	0.00	0.45	1.01
Realistic	$ICE3$-R	0.05	0.20	0.47	0.49	0.10	0.80	CCD-R	0.20	0.23	1.72	3.02	0.32	1.13
Realistic PDF+PS	$ICE3$-A	0.05	0.20	0.47	0.50	0.12	1.00	CCD-A	0.20	0.24	1.71	3.02	0.31	1.00
Gaussian PDF+PS	$ICE3$-G	0.05	0.23	0.44	0.01	0.11	1.00	-	-	-	-	-	-	-

2.2 Direct numerical simulation

Direct numerical simulations are carried out in a fully developed turbulent channel bounded by roughness as illustrated in Fig. 2. The Navier-Stokes equation and the energy conservation equation for the temperature field
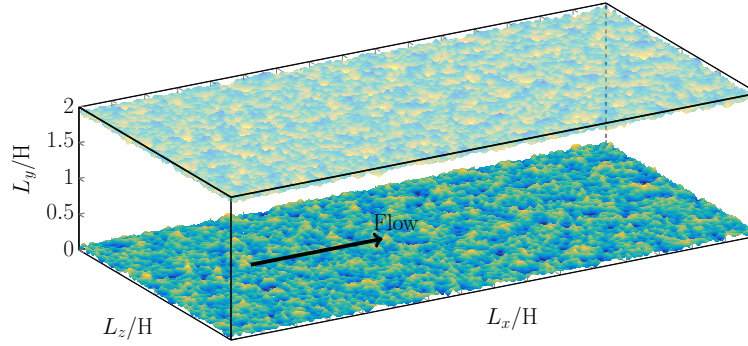
Fig. 2 Schematic representation of simulation domain with an exemplary pseudo-realistic surface mounted on the channel walls. H denotes the channel half height.

θ as a dimensionless passive scalar writes:

$$\boldsymbol{\nabla} \cdot \mathbf{u} \;=\; 0, \tag{1}$$

$$\frac{\partial \mathbf{u}}{\partial t} + \boldsymbol{\nabla} \cdot (\mathbf{uu}) \;=\; -\frac{1}{\rho}\boldsymbol{\nabla}p + \nu\nabla^2\mathbf{u} - \frac{1}{\rho}P_x e_x + \mathbf{f}_{\mathrm{IBM}}, \tag{2}$$

$$\frac{\partial \theta}{\partial t} + \nabla \cdot (\mathbf{u}\theta) \;=\; \alpha\nabla^2\theta + Q + \mathbf{f}_\theta, \tag{3}$$

where ρ, ν, α represent the density, the kinematic viscosity and the thermal diffusivity of the flow, respectively. The double-averaged velocity and temperature profiles in wall-parallel directions and time are denoted as U and Θ for the sake of simplicity. The source term Q is added to the energy equation for the simulation of mixed-type thermal boundary condition [22]. The roughness with no-slip boundary and zero-temperature boundary conditions are realized by imposing immersed boundary method (IBM) following Goldstein *et al.* [23]. Thus, external source terms for momentum ($\mathbf{f}_{\mathrm{IBM}}$) and energy ($\mathbf{f}_\theta$) are added in the corresponding equation. The Prandtl number $Pr = 0.71$ is selected for simulating air flow. Under the consideration of the excessive computational cost required by conventional DNS, minimal channel DNS (denoted as *Mini*) is employed in the most cases in the present work. It is shown that with a reduced simulation spanwise size the turbulent flow in the near wall region up to the critical height $y_c^+ = 0.4L_z^+$ can be still considered as 'healthy turbulence' [24] and thus the mean velocity and temperature profiles would collapse for minimal or full-size simulation below the critical height. The physical scaling of the channel half height H is selected for each case individually to achieve a clear separation of length scales H and k while maintaining a significant roughness effect within the currently investigated range of Re$_\tau$. The largest and the smallest roughness wavelengths λ_0 and λ_1 of each type of roughness are selected to cover the roughness scales that are influential for the roughness effect on the temperature and flow field. The minimal channel size is selected to accommodate for the largest roughness wavelength λ_0. Based on the constraints, the simulation configurations selected for each case are listed in table 2.

3. RESULTS

3.1 Global flow statistics

The Nusselt number ($Nu = 4Hq_w/\Theta_m\lambda$) as well as the Reynolds analogy ($RA = 2St/C_f$) are investigated in the present section, where $C_f = 2\tau_w/\rho U_b^2 = 2/U_b^{+2}$ is the skin friction coefficient, and $St = 1/U_b^+\Theta_m^+$

Table 2 Simulation configurations. * is the wildcard that represents R (realistic), A (artificial) and G (Gaussian) case. The wavelength boundaries are not given for $ICE4$-AA due to surface anisotropy.

| Roughness	H, [mm]	L_x/H	L_z/H	λ_0/H	λ_1/H	Roughness	H, [mm]	L_x/H	L_z/H	λ_0/H	λ_1/H
$ICE1$-* (Mini)	5	4.0	0.8	0.8	0.06	$Sand$-R (Full)	12.8	5.5	3.9	0.8	0.02
$ICE2$-* (Mini)	5	4.0	0.8	0.8	0.02	$Sand$-A (Full)	12.8	6.3	3.1	0.8	0.02
$ICE3$-* (Mini)	5	4.0	0.8	0.8	0.06	$Sand$-* (Mini)	12.8	4.0	0.8	0.8	0.02
$ICE4$-* (Mini)	5	4.0	0.8	0.8	0.02	CCD-R/A (Full)	10	6.0	4.0	4	0.05
$ICE4$-AA (Mini)	5	6.8	0.8	-	-						
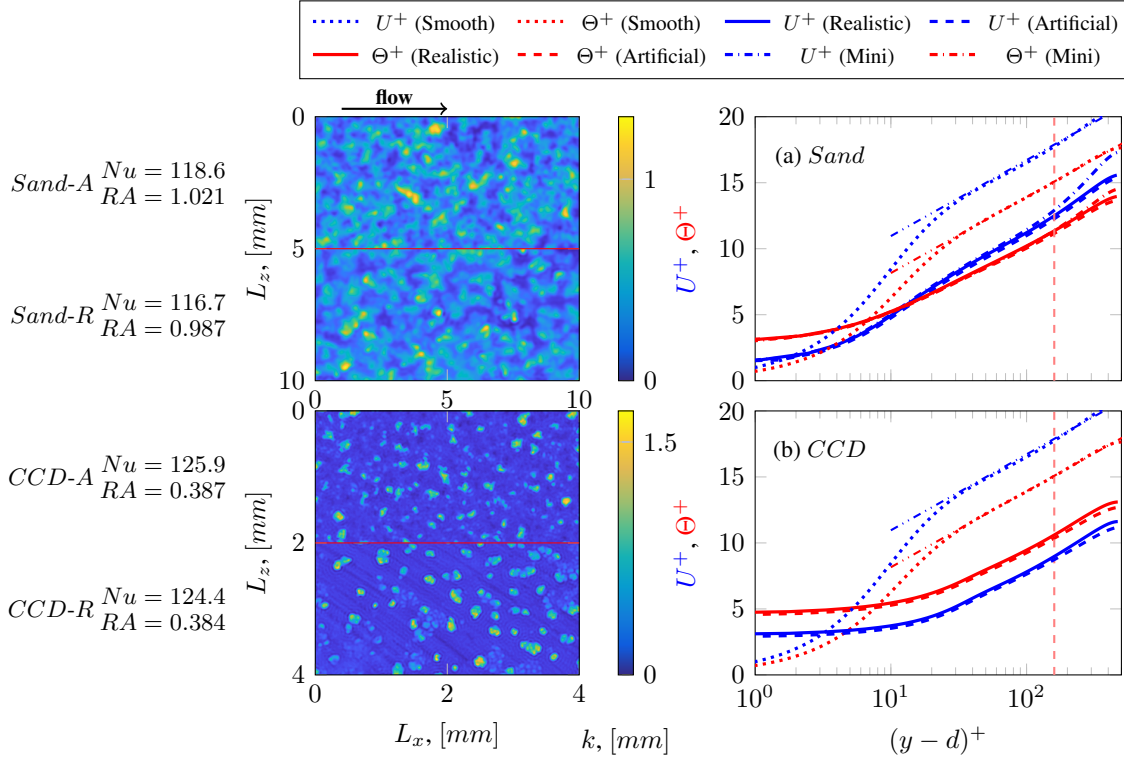
Fig. 3 Mean velocity and temperature profiles of (a): $Sand$ and (b): CCD at $\mathrm{Re}_\tau = 500$. The critical height y_c^+ for the minimal channel is marked with red vertical dashed line. The corresponding roughness are shown on the left column.

represents the Stanton number. The heat flux across the rough wall is defined with q_w and the mixed mean temperature [25] is $\Theta_m = \int_0^{2H} U(\Theta - \Theta_w)\mathrm{d}y / \int_0^{2H} U\mathrm{d}y$, where Θ_w represents the wall temperature, λ denotes thermal conductivity, τ_w is the wall shear stress and $U_b = 1/H \int_0^H U\mathrm{d}y$ is the bulk mean velocity. Please note that the global flow statistics can be evaluated only in full-sized DNS simulations due to the deviation of flow statistics in minimal-channel DNS in the outer flow region. Due to the computational constraints, full-span DNSs at $\mathrm{Re}_\tau = 500$ are performed only for two cases, namely $Sand$ and CCD.

The mean velocity and temperature profiles are plotted in figure 3. The corresponding global statistics are documented in the figure as well. The virtual origin of the rough wall is determined by the zero-plane displacement d following Jackson's method [26]. Excellent collapse of the profiles are achieved by the artificial surrogates with their target realistic counterparts. The agreement of the temperature and velocity profiles leads to successful reproduction of the Nu and RA values of the artificial surrogates with discrepancies less than 4%. Moreover, the minimal channel DNS results for $Sand$-R is additionally illustrated in figure 3 with dash-dotted lines to validate the performance of minimal channels. It is obvious that the mean temperature and velocity profiles of minimal channel agree well with the full-span channel profiles up to $y_c^+ = 160$.
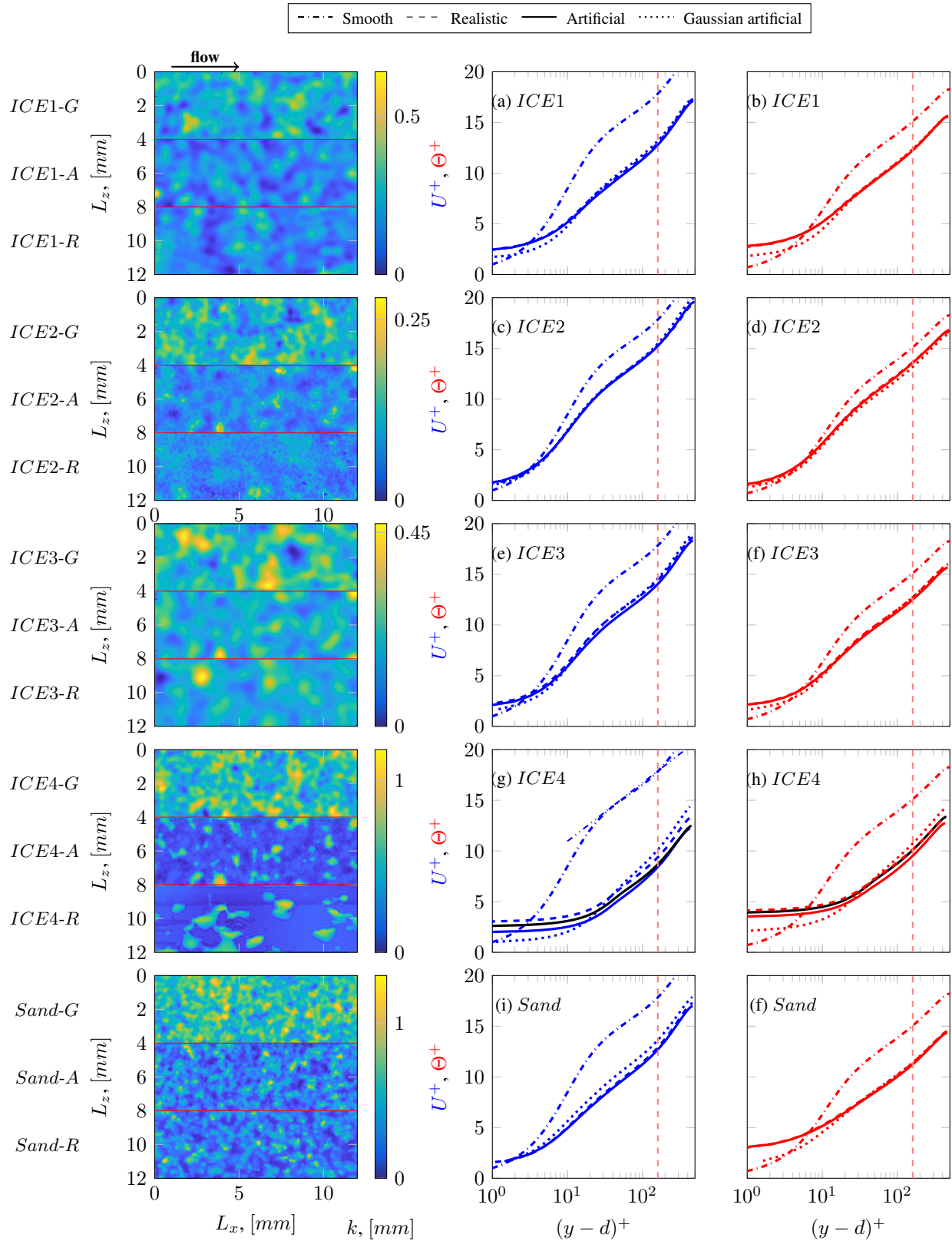
Fig. 4 Mean velocity (a,c,e,g,i) and mean temperature (b,d,f,h,f) profiles of different roughness at $\mathrm{Re}_\tau = 500$ in minimal channels. The vertical dashed line represents the critical height of the minimal channel $y_c^+ = 160$. The corresponding rough surfaces are shown on the left panel. The temperature log-law is based on Kader [27]. $ICE4$-AA is represented by black solid lines in (g,h)
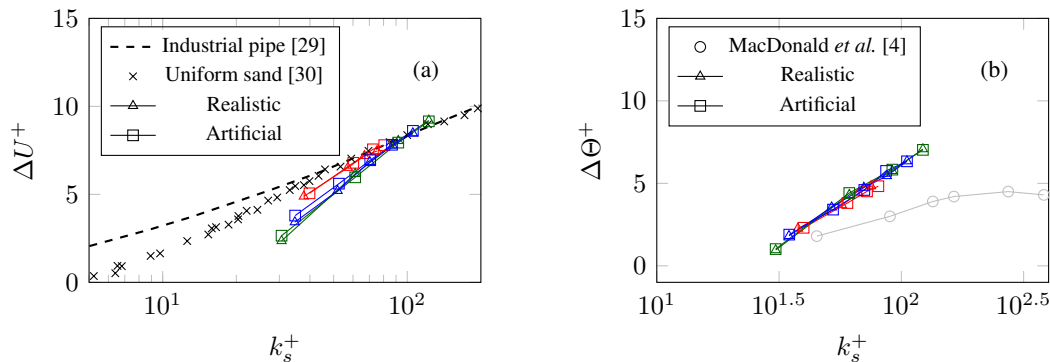
Fig. 5 Roughness functions (a) and temperature roughness functions (b) of different roughness as functions of k_s^+. Red: $ICE1$ ($k_s = 0.38mm$ vs. $0.40mm$), green: $ICE2$ ($k_s = 0.30mm$), blue: $ICE3$ ($k_s = 0.35mm$).

3.2 Mean velocity and temperature profiles

The inner-scaled mean velocity and temperature profiles of all artificial roughness in minimal channels, i.e. $ICE1$-A/G to $ICE4$-A/G and $Sand$-A/G at $\mathrm{Re}_\tau = 500$ are illustrated in figure 4. The reference original roughness are additionally included in each plot with dashed lines. It is evident that the artificial surrogates successfully recover the temperature and velocity profiles of their target roughness. The only exception can be observed for $ICE4$-A due to the violation of the isotropic assumption for the realistic surface as is reflected by its SAR$\approx$1.7. Significant larger downward shift of both Θ^+ and U^+ profiles can be observed compared to the $ICE4$-R. This is in line with the observations by Busse *et al.* [21].In light of this, $ICE4$-A is stretched in streamwise direction to obtain SAR value consistent with its original surface, i.e. stretching the streamwise extend by 1.7 times. This surface is denoted as $ICE4$-AA. Based on the simulation results shown in figure 4(g,h) with black solid lines, the temperature profile of $ICE4$-AA successfully reproduces the realistic profile, while the velocity profile still fails to collapse to the realistic roughness. This may be due to the fact that the target PS for the roughness surrogate is radially averaged and the flow field is more sensitive to the change of roughness undulation due to its crucial impact to the pressure drag term in the momentum equation [4]. On the other hand, interesting behavior of the Gaussian artificial surfaces can be observed. Generally the effect of Gaussian surfaces is dominant below the roughness crest, which may be predominantly due to the varied blockage effect.Nevertheless, this effect is weaker in the outer-layer, e.g. in the logarithmic layer, which results in almost identical ΔU^+ compared with the artificial surrogates. For $\Delta\Theta^+$ the effect of substituting PDF in the outer-layer is even less pronounced. Based on the present observations, it is clear that at lower ES, the effect of changing PDF is insignificant, while for $Sand$ cases, considerable decrease of ΔU^+ can be observed for the Gaussian variation. However, taking the temperature field into account, it is clear that the major source of the effect for changing PDF can be accounted for the pressure drag of the surface. For a surface with low ES, the partition of pressure drag is lower, thus the variation of the abundance of the roughness peaks – which is controlled by PDF – may manifest into a smaller impact on the flow field. In order to investigate the influences of different roughness statistics on $\Delta\Theta^+$ in an isolated manner, the $\Delta\Theta^+$ for all investigated cases at $\mathrm{Re}_\tau = 500$ is plotted as a function of $k_{\mathrm{rms}}/\mathrm{H}$, Sk and ES in figure 6. Monotonic increase of $\Delta\Theta^+$ with $k_{\mathrm{rms}}/\mathrm{H}$ can be observed in figure 6(a). Among the investigate cases except $ICE4$, both artificial and Gaussian roughness collapse well to their realistic counterparts. This indicates the crucial role of $k_{\mathrm{rms}}/\mathrm{H}$ for scaling the $\Delta\Theta^+$ value. Nonetheless, an obvious scatter of $\Delta\Theta^+$ can be observed in figure 6(b), indicating a weaker impact of Sk on the roughness heat transfer ability. The effect of ES is illustrated in figure 6(c), the clear trend of the $\Delta\Theta^+$ distribution confirms the influence of ES for the roughness thermohydraulic properties. A peak $\Delta\Theta^+$ value is achieved at ES$\approx$ 0.35, this may probably be attributed to the change from wavy to dense roughness regime with increasing ES value [28]. However, to shed more light into the mechanism of how ES affects $\Delta\Theta^+$, a systematic study of the roughness regimes in terms of heat transfer is required in future work.
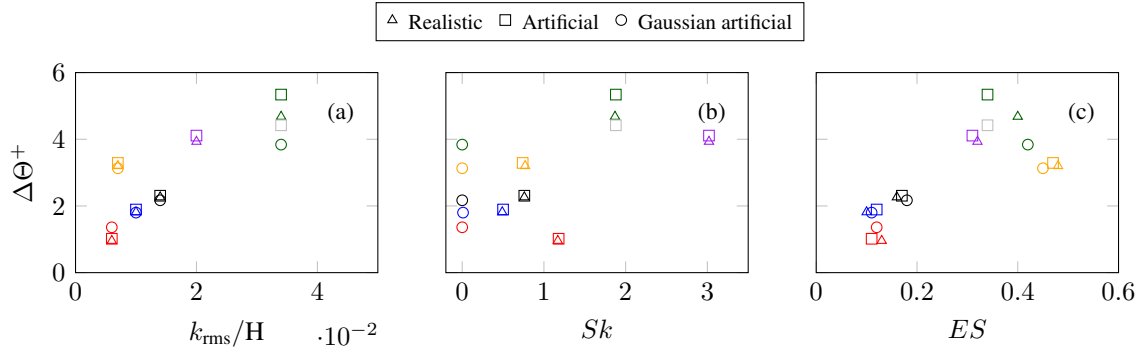
Fig. 6 Dependence of the temperature roughness function $\Delta\Theta^+$ at $\mathrm{Re}_\tau = 500$ on (a) $k_\mathrm{rms}/\mathrm{H}$, (b) Sk and (c) ES. Black: $ICE1$, red: $ICE2$, blue: $ICE3$, green: $ICE4$, orange: $Sand$, purple: CCD. Additionally $ICE4\text{-}AA$ is represented by the gray square.

Furthermore, based on the satisfactory results for $ICE1\text{-}A$ to $ICE3\text{-}A$, these surfaces are simulated at higher $\mathrm{Re}_\tau = 500 - 2000$ to approach fully rough regime. The ΔU^+ and $\Delta\Theta^+$ values are plotted in figure 5 as functions of equivalent sand grain size k_s. The k_s values of each roughness are obtained by fitting the current data in the fully rough regime with the asymptotic roughness function by Nikuradse [30]. The calculated k_s values for each case are documented in the caption of figure 5 and $\Delta\Theta^+$ as functions of k_s^+ is shown in figure 5(b). For comparison, the data by Macdonald *et al.* [4] is added to the plot. Obvious steeper increase of $\Delta\Theta^+$ for present rough surfaces may be attributed to the multi-scale nature of the currently investigated roughness – smaller roughness structures start to behave as thermally rough and contribute to the heat transfer as the Re_τ increases. This may also explain the absence of the saturation of $\Delta\Theta^+$ in the fully rough regime observed from sinusoidal roughness [4], since the realistic roughness may include length scales smaller than k_s and consequently delay the saturation of $\Delta\Theta^+$.

3.3 Correlation between temperature and velocity fluctuations

The temperature-velocity correlations of all investigated cases at $\mathrm{Re}_\tau = 500$ are visualized in figure 7. In the figure, solid and dashed lines represent artificial surrogates and realistic roughness, respectively. The Gaussian artificial surfaces are illustrated by dotted lines. It can be observed that for almost all artificial surrogates, excluding $ICE4\text{-}A$, exhibit excellent collapse to their target roughness. The Gaussian roughness apparently fails to reproduce the temperature fluctuations. Moreover, the temperature-velocity correlations for stretched $ICE4\text{-}AA$ is included in figure 7(d) with square symbols. As can be observed, the anisotropic surrogate exhibits closer roughness effect to its target. Nevertheless, the discrepancies of the profiles still indicate the need of further modifications for generating anisotropic roughness surrogates.

4. CONCLUSION

In the present work we examine the possibility of reproducing realistic rough surfaces based on the PDF and PS of a realistic roughness topography in order to flexibly substitute real roughness samples with surrogates and characterize their thermohydraulic effect on turbulent flows. Six types of realistic surfaces from different engineering backgrounds are incorporated: ice accretion on aero-engine (ICE), sandpaper ($Sand$) and combustion chamber deposit roughness (CCD). Direct numerical simulations are carried out with the artificially reproduced surface surrogates at a range of $\mathrm{Re}_\tau = 500 - 2000$. The surrogates successfully reproduced the thermohydraulic properties of their corresponding target realistic roughness under the premise of surface isotropy as reflected by the collapse of mean profiles as well as the Nu and RA values. Moreover, the equivalent sand grain height k_s is accurately recovered by the surrogates for $ICE1\text{-}A$ to $ICE3\text{-}A$. Based on the investigation of $\Delta\Theta^+$, the crucial roles of k_rms and ES for characterizing the thermohydraulic properties of the
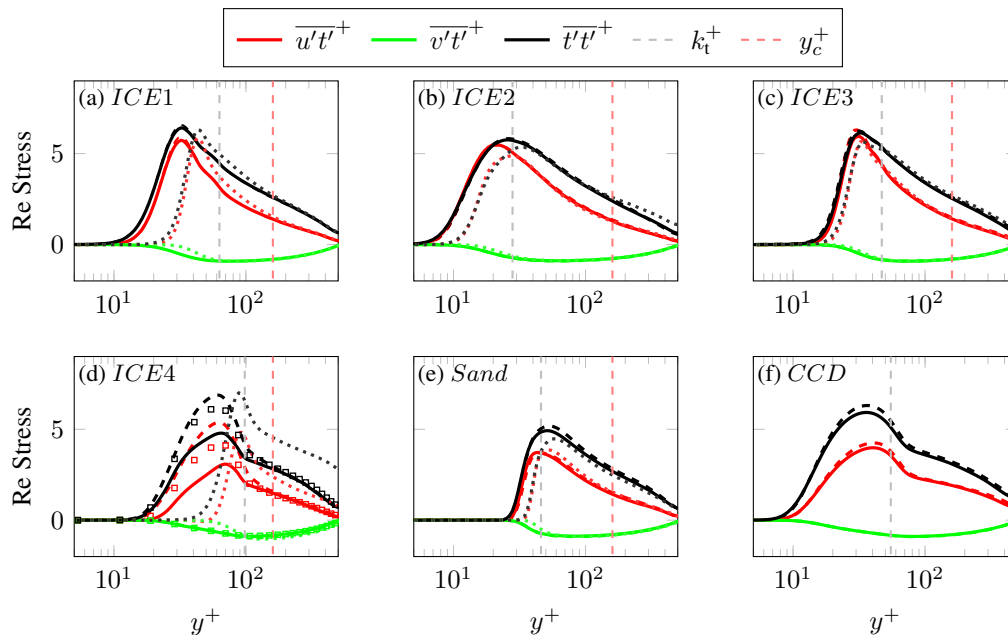
Fig. 7 Temperature-velocity correlations of ICE-1 to ICE-4, $Sand$ and CCD at $Re_\tau = 500$. The gray vertical dashed line represents k_t^+ of realistic surfaces, the red vertical dashed represents y_c^+ of the minimal channels. Solid line: artificial, dashed line: realistic, dotted line: Gaussian. In (d), $Sand$-AA is included in the (d) with square symbols.

roughness are illustrated. Finally, it is shown that the correlation between temperature and velocity fluctuations is successfully reproduced by the surrogates. The satisfactory results highlight the promising capability of the currently investigated roughness characterization method based on the roughness PDF and PS. By comparing anisotropic roughness with its isotropic surrogate, the impact of streamwise surface anisotropy is observed to results in lower ΔU^+ and $\Delta \Theta^+$ values. Surface stretching based on the desired SAR value is applied to generate the anisotropic roughness surrogate $ICE4$-AA. Collapse of the temperature profiles is achieved by $ICE4$-AA while this surface fails to reproduce the velocity field of the target roughness.

ACKNOWLEDGMENTS

REFERENCES

[1] Townsend, A. A. (1976) The structure of turbulent shear flow / A.A.Townsend, Cambridge University Press Cambridge [Eng.] ; New York, 2nd ed. edition.

[2] Perry, A. E. and Joubert, P. N. (1963) Rough-wall boundary layers in adverse pressure gradients. *Journal of Fluid Mechanics,* **17**(2), 193–211.

[3] Yaglom, A. and Kader, B. (1974) Heat and mass transfer between a rough wall and turbulent fluid flow at high Reynolds and Péclet numbers. *Journal of Fluid Mechanics,* **62**(3), 601 – 623.

[4] MacDonald, M., Hutchins, N., and Chung, D. (2019) Roughness effects in turbulent forced convection. *Journal of Fluid Mechanics,* **861**, 138–162.

[5] Flack, K. A. (2018) Moving beyond Moody. *Journal of Fluid Mechanics,* **842**, 1–4.

[6] Forooghi, P., Stroh, A., Magagnato, F., Jakirlić, S., and Frohnapfel, B. (08, 2017) Toward a Universal Roughness Correlation. *Journal of Fluids Engineering,* **139**(12) 121201.

[7] NAPOLI, E., ARMENIO, V., and DE MARCHIS, M. (2008) The effect of the slope of irregularly distributed roughness elements on turbulent wall-bounded flows. *Journal of Fluid Mechanics,* **613**, 385–394.

[8] Barros, J. M., Schultz, M. P., and Flack, K. A. (2018) Measurements of skin-friction of systematically generated surface roughness. *International Journal of Heat and Fluid Flow,* **72**, 1 – 7.

[9] Busse, A., Lützner, M., and Sandham, N. D. (2015) Direct numerical simulation of turbulent flow over a rough surface based on a surface scan. *Computers & Fluids,* **116**, 129 – 147.

[10] Yang, J., Stroh, A., Chung, D., and Forooghi, P. (2022) Direct numerical simulation-based characterization of pseudo-random roughness in minimal channels. *Journal of Fluid Mechanics,* **941**, A47.

[11] Bons, J., Taylor, R., McClain, S., and Rivir, R. (2001) The many faces of turbine surface roughness. In *ASME Turbo Expo 2001: Power for Land, Sea, and Air* American Society of Mechanical Engineers pp. 739–748.

[12] Bons, J. (2005) A critical assessment of Reynolds analogy for turbine flows. *J. Heat Transfer,* **127**(5), 472–485.

[13] Bons, J. P. and McClain, S. T. (09, 2004) The Effect of Real Turbine Roughness With Pressure Gradient on Heat Transfer . *Journal of Turbomachinery,* **126**(3), 385–394.

[14] Forooghi, P., Stripf, M., and Frohnapfel, B. (12, 2018) A systematic study of turbulent heat transfer over rough walls. *International Journal of Heat and Mass Transfer,* **127**, 1157–1168.

[15] Jelly, T. O. and Busse, A. (2018) Reynolds and dispersive shear stress contributions above highly skewed roughness. *Journal of Fluid Mechanics,* **852**, 710–724.

[16] Flack, K. A., Schultz, M., and Barros, J. (2020) Skin Friction Measurements of Systematically-Varied Roughness: Probing the Role of Roughness Amplitude and Skewness. *Flow, Turbulence and Combustion,* **104**(2-3), 317–329.

[17] Pérez-Ràfols, F. and Almqvist, A. (2019) Generating randomly rough surfaces with given height probability distribution and power spectrum. *Tribology International,* **131**, 591 – 604.

[18] Bansmer, S., Baumert, A., Sattler, S., Knop, I., Leroy, D., Schwarzenboeck, A., Jurkat-Witschas, T., Voigt, C., Pervier, H., and Esposito, B. (2018) Design, Construction and Commissioning of the Braunschweig Icing Wind Tunnel. *Atmospheric Measurement Techniques,* **11**, 3221–3249.

[19] Velandia., J. S. and Bansmer, S. E. (2020) Detailed atmospheric ice accretion surface measurement using micro-computed tomography. *Atmospheric Science Letters,* **21**(10), e997.

[20] Forooghi, P., Weidenlener, A., Magagnato, F., Böhm, B., Kubach, H., Koch, T., and Frohnapfel, B. (2018) DNS of momentum and heat transfer over rough surfaces based on realistic combustion chamber deposit geometries. *International Journal of Heat and Fluid Flow,* **69**, 83 – 94.

[21] Busse, A. and Jelly, T. (2019) Influence of surface anisotropy on turbulent flow over irregular roughness. *Flow Turbulence Combust,* **104**, 331–354.

[22] Kasagi, N., Tomita, Y., and Kuroda, A. (08, 1992) Direct Numerical Simulation of Passive Scalar Field in a Turbulent Channel Flow. *Journal of Heat Transfer,* **114**(3), 598–606.

[23] Goldstein, D., Handler, R., and Sirovich, L. (1993) Modeling a no-slip flow boundary with an external force field. *J. Comput. Phys.,* **105**(2), 354–366.

[24] Chung, D., Chan, L., MacDonald, M., Hutchins, N., and Ooi, A. (2015) A fast direct numerical simulation method for characterising hydraulic roughness. *Journal of Fluid Mechanics,* **773**, 418–431.

[25] Pirozzoli, S., Bernardini, M., and Orlandi, P. (2016) Passive scalars in turbulent channel flow at high Reynolds number. *J. Fluid Mech.,* **788**, 614–639.

[26] Jackson, P. S. (1981) On the displacement height in the logarithmic velocity profile. *Journal of Fluid Mechanics,* **111**, 15–25.

[27] Kader, B. A. (1981) Temperature and concentration profiles in fully turbulent boundary layers. *International Journal of Heat and Mass Transfer,* **24**(9), 1541–1544.

[28] Schultz, M. P. and Flack, K. A. (2009) Turbulent boundary layers on a systematically varied rough wall. *Physics of Fluids,* **21**(1), 015104.

[29] Moody, L. (1944) Friction factors for pipe flow. *Trans. ASME,* **66**(8), 671–677.

[30] Nikuradse, J. (1933) Stroemungsgesetze in rauhen Rohren, VDI-Verl., Berlin.